POLITECNICO DI TORINO
Repository ISTITUZIONALE

Modelling and simulation of a tethered UAS

(Article begins on next page)

02 May 2024

Modelling and simulation of a tethered UAS*

Emilio Dicembrini[1], M. Scanavino[2], F. Dabbene[3] and G. Guglieri[2]

Abstract—Battery lifetime is one of the most challenging problems for Unmanned Aircraft System (UAS) applications. Multi-rotor platforms usually suffer limited payload capabilities and flight time. To overcome this problem, tethered vehicle solutions have been developed. In this paper, we propose a mathematical model able to describe the dynamic behaviour of a tethered UAS. The approach is based on the Finite Element Method and Lagrange's Equation of motion. The cable is divided into segments linked to each other by spherical joints. An additional virtual element is used to represent the vehicle dynamics. Compared to other works, a variable cable length is implemented as well as wind effects on overall system are included. Simulation results corroborate that the proposed approach is able to simulate how the cable and UAS work in different operating conditions, such as take-off and hovering in both still air and wind scenario.

I. INTRODUCTION

In the past years the use of Unmanned Aircraft Systems (UAS) has become widespread. In particular, multirotor vehicles have gain momentum and today they are able to support or even substitute traditional air vehicles in both civil and military applications [1]. The reason can be summarized in three aspect: Vertical Take-Off and Landing (VTOL) capability, simplified propulsion system and reduced flight control complexity. The technology level reached by autopilot control boards, as well as sensor miniaturization and cost reduction have enabled a lot of applications in which Unmanned Aerial Vehicles (UAVs) can get involved. Considering commercial operations, precision farming, photogrammetry as well as delivery are typical examples in which unmanned systems provide benefits thanks to their flexibility and low cost. Many research activities ([2], [3], [4]) exploit UAS platforms for monitoring purposes such as air pollution tracking, traffic management or water river analysis.

Battery lifetime is one of the main limitation when considering rotary wing UAS operations. Moreover, unlike fixed wing architecture, multi-rotor vehicles are affected by a lower aerodynamic efficiency, resulting in limited flight time or payload capabilities. Different solutions have been proposed in literature to overcome this challenge. As reported by [5], solar cells and hydrogen fuel cells are possible alternatives to replace LiPo batteries. Solar cells are preferred for fixed wing UAV due to wide wing surface [6]; on the other hand, the total weight of a hydrogen fuel cell system (7 kg) would be reasonable for UAS with a maximum take off in the range from 10 kg to 35 kg [7]. The complexity of a hydrogen fuel cell propulsion system (tank, fuel, cooling and management) would not be suitable for small scale vehicles.

A promising solution to increase the energy available onboard UAVs is to power the vehicle with a cable from ground. Tethered UAS can exploit a virtually unlimited flight time. Moreover, a secure and stable data transmission is possible as no radio link is required. On the other hand, the main disadvantage is related to the limited flight range. However, for monitoring or surveillance applications where endurance is the driving requirement, tethered UAS have great potential. This is further enhanced by industrial platforms commercially available in the market: Aquila 100 by Eagle Sky Light [32] or Orion by Elistair are just a few examples.

The main objective of this work is the preliminary modelling and simulation of a tethered UAS to investigate the cable and vehicle dynamics. In literature, several works concerning the dynamic modelling and simulation of tethered underwater robots are available. Choo and Casarella in [9] present different approaches to describe tethered underwater systems. They identify the Finite Element Method as the most versatile. It can be used to simulate whatever unsteady cable's motion. The elements of the cable can be modelled as a rigid or extensible thin rod lumped mass. Newton's law ([28]) or Lagrange's Equation ([18], [21]) are the primary way to derive the dynamic equations. Another method is based on the fundamental equations of structural mechanics. The tension along the cable is given as function of the longitudinal strain ([27], [30], [29], [31]). In this case, the Hooke's law is commonly leveraged. This can be used to represent unsteady cable motion; however, due to the complexity of the problem this simplification is not always suitable and other constitutive laws must be adopted. Sometimes, the Linearization Method can be exploited to simulate small deviations from an equilibrium state ([15], [23]). However, this solution does not fulfill the purpose of the present work. Finally, it is possible to describe the cable neglecting its mass. In this approach, the degree of freedom are the cable's stretch and its orientation as reported in [25] and [26]. As a result, the cable is modelled as a single elastic element between the vehicle and the attachment point.

In this paper we propose a mathematical model able to simulate the dynamic behaviour of the cable and the tethered UAS. Compared to other works where the cable has a fixed length, we provide a solution to describe the cable

[1]Emilio Dicembrini is with the Department of Electronics and Telecommunications, Politecnico di Torino, Turin, Italy `emilio.dicembrini@studenti.polito.it`

[2] Department of Mechanical and Aerospace Engineering, Politecnico di Torino, Turin, Italy `matteo.scanavino@polito.it` `giorgio.guglieri@polito.it`

[3] Institute of Electronics, Computer and Telecommunication Engineering, National Research Council of Italy, Turin, Italy `fabrizio.dabbene@ieiit.cnr.it`

unwinding. Based on the work in [24], our model is able to simulate the complete dynamic system (cable and UAV) in a three dimensional space. Moreover, we introduce the effect of wind force in both UAS and cable. Simulations results are discussed to evaluate the overall system behaviour in wind and still air conditions. The overall system modelling is presented in Section II where the focus is given to the Finite Element Method, the reference systems as well as variable cable length and UAV model. Section III provides details on Lagrange's Equation approach, including assumptions and related simplifications owing to the reference systems adopted. Moreover, the aerodynamic forces acting on the cable and UAS are presented to the reader. Simulation results are discussed in Section IV. Take-off and hovering in still air and wind conditions are simulated to corroborate the proposed approach. Conclusions and future works are reported in Section V.

Fig. 1: Tethered UAS by Eagle Sky Light [32]

II. SYSTEM MODELLING

The dynamic modelling of the cable leverage the Finite Elements Method (FEM) as proposed in [9]. The cable is divided into n segments linked to each other at their extremities by a spherical joint. These points are called nodes. The spherical joints allow the exchange of forces between contiguous elements. Based on the assumption of an in-extensible cable, each segment of the cable is modelled as a weightless rigid rod and a lumped mass to its extremity as in Figure 2. The cable is considered as a system of n rigid bodies connected end to end, with the first element bound to the ground. Figure 3 shows schematically a cable subdivision in three elements. An inertial reference system is fixed in the connection point between the cable and ground; moreover, for each segment a local reference frame is defined. The UAS dynamics is solved simultaneously with the cable. The aerial vehicle is modeled as a virtual segment of the cable,

as proposed in [21], so that the overall system (cable and UAS) is made by $(n+1)$ elements. The virtual segment, corresponding to the UAS, is connected to the last element of the cable. The length of this virtual element is equal to the distance between the connection point and the center of mass of unmanned aerial vehicle. Moreover, the inertial properties of the virtual element correspond to the mass and moment of inertia of the UAS. Each element of the cable is linked to the preceding one by a spherical joint, which allows free rotation without translation in any direction. For this reason, the whole system (cable and UAS) has $3(n+1)$ degree of freedoms (DOFs).
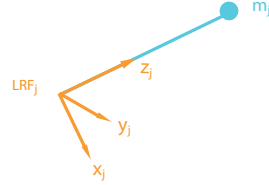

Fig. 2: Isolated cable element with its local reference frame and lumped mass to the extremity.

A. Reference Systems

The Inertial Reference Frame (IRF), labeled XYZ, is centered on the link between the first element of the cable and the ground. For each segment of the cable, a Local Reference Frame (LRF) xyz is defined with the $z-axis$ aligned along the axial direction of the element. In this local frame the lumped mass is located in $(0,0,l)$, where l is the length of the element. The rigid body orientation is represented by means of Euler Angles. The LRF orientation is obtained with three successive rotations starting from the IRF. The first rotation is above the inertial reference frame X axis of an angle ϕ to achieve the rotated reference frame $x'y'z'$. This intermediate reference system is rotated by an angle θ around the y' axis obtaining the RF $x''y''z''$. Finally the LRF xyz is achieved rotating the previous RF above the
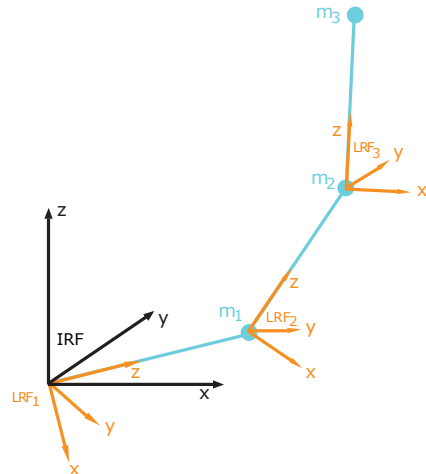

Fig. 3: Example of cable subdivision in three elements.

z'' axis by an angle ψ (Figure 4). Gimbal lock occurs when $\theta = \pm\frac{\pi}{2}$ [19]. This condition corresponds to the $z-axis$ of the local reference frame parallel to the XY plane. In other words, the cable is placed on the ground or the UAS propeller plane is perpendicular to ground.

The rotational matrix which transforms the j-th local RF into the inertial RF is $R_{\phi\theta\psi} = R_\phi R_\theta R_\psi$, where R_ϕ, R_θ and R_ψ are the individual matrix corresponding to the rotations previously described. Recalling that the origin of the $(j+1)^{th}$ RF is centered on the jth lumped mass m_j, the coordinate of the kth segment lumped mass can be expressed in the inertial RF as in Equation 1.
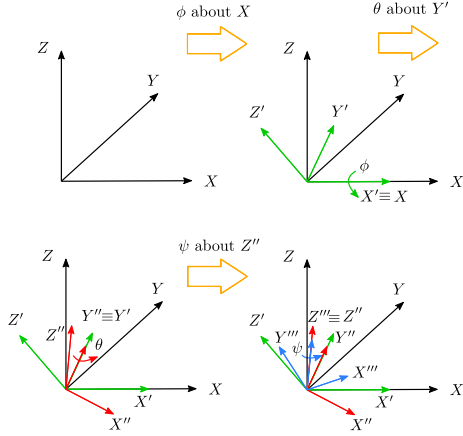

Fig. 4: Euler angles and reference system rotation.

$$\begin{pmatrix} X_k \\ Y_k \\ Z_k \end{pmatrix} = \sum_{j=1}^{k} R_{\phi_j\,\vartheta_j\,\psi_j}^{-1} \begin{pmatrix} 0 \\ 0 \\ l_j \end{pmatrix} \qquad k=1,\ldots,n+1 \qquad (1)$$

Equation 1 is in its general form; exploiting the chosen LRF, the position of the kth lumped mass is independent from the angle ψ as reported in Equation 2.

$$\begin{cases} X_k = \sum_{j=1}^{k} -l_j\,s_{\vartheta_j} \\ Y_k = \sum_{j=1}^{k} -l_j\,s_{\phi_j}\,c_{\vartheta_j} \qquad k=1,\ldots,n+1 \qquad (2) \\ Z_k = -\sum_{j=1}^{k} l_j\,c_{\phi_j}\,c_{\vartheta_j} \end{cases}$$

B. Variable Cable Length

In order to model a variable cable length, the dimension of the first segment is set as a function of time, $l_1 = l_1(t)$. All the other segments have fixed length equal to l. l_1 is bounded between l_{min} and l_{max}. When the UAS is climbing, the cable length will increase. As l_1 reaches l_{max} a new element is added in the cable model. Vice versa, when the UAS is landing, the cable length is reduced by removing the first element as soon as l_1 reaches l_{min}. Our method is the same as reported in [24]; however, we extended the formulation for a three dimensional problem representation. This approach guarantees an easier derivation of the Lagrange's Equations,

since only the length of one element is function of time:

$$\dot{l}_1 = \frac{dl_1}{dt} \neq 0$$

$$\ddot{l}_1 = \frac{d^2 l_1}{dt^2} \neq 0$$

The first segment velocity and its acceleration are supposed known. In this way a winch model can be implemented separately from the cable/UAV system with a feedback of the force acting from the cable to the drum. This solution is configurable for different winch models.

C. Simplified UAS model

The unmanned aerial vehicle is modelled as a virtual element of the cable. As previously explained, the length of this virtual element is equal to the distance between the center of mass of the UAS and the connection point with the last segment of the cable. The inertial properties of the UAS are applied to the virtual elements, including mass and inertia. Thrust generated by the UAS propellers are introduced into the model as external forces acting along the z-axis of the UAS LRF. The thrust of each propeller is computed leveraging the Blade Element Theory (BET) (et. al [12], [11]), while brushless motors are modelled as simple first order mechanical systems. The dynamics of the electric motors are neglected since they are much faster than the mechanical one.

Moments acting on the x and y UAV axes are calculated considering the differential thrust generated by the propellers, assuming a *X* vehicle configuration. The moment respect the Z axis is equal to the sum of the reaction moments from the propellers to the motors ([11]).

Altitude and attitude controllers are included in the model. A Proportional, Integrative and Derivative (PID) control algorithm is used to keep a stable attitude and the desired altitude. The controllers compute the required a thrust and moments and transform them into set-point angular speeds for each motors to reach the references.

III. LAGRANGE'S EQUATIONS

To compute the dynamic behaviour of the cable, the Lagrange's Equation approach is leveraged as in Eq. 3.

$$\frac{d}{dt}\left(\frac{\partial \mathscr{L}}{\partial \dot{q}_i}\right) - \frac{\partial \mathscr{L}}{\partial q_i} = Q_i' \qquad (3)$$

where q_i are the generalized coordinates, Q_i' are the generalized forces and, $\mathscr{L} = E_{kinetic} - E_{potential}$. The total kinetic energy is given by the sum of translational and rotational terms.

A. Potential Energy

Based on the assumption of null potential energy in the XY-plane ($Z=0$), the total potential energy of the multi-body system is:

$$E_{potential} = \sum_{k=1}^{n+1} m_k Z_k g \qquad (4)$$

where m_k is the mass of the kth cable segment and Z_k is its elevation with respect to the inertial RF. Recalling that the potential energy Eq. (4) depends only on the position of the lumped cable mass segment, Equation (3) can be rearranged as in Eq. (5).

$$\frac{d}{dt}\left(\frac{\partial E_{kinetic}}{\partial \dot{q}_i}\right) - \frac{\partial E_{kinetic}}{\partial q_i} = Q'_i - \frac{\partial E_{potential}}{\partial q_i} \qquad (5)$$

where Q_i is defined in Eq. 6.

$$Q_i = Q'_i - \frac{\partial E_{potential}}{\partial q_i} \qquad (6)$$

B. Translational Kinetic Energy

The translational kinetic energy of the multi-body system is sum of the translational kinetic energy of its elements.

$$E_{trans} = \frac{1}{2}\sum_{k=1}^{n+1} m_k \left|\vec{V}_k\right|^2, \qquad (7)$$

where $\vec{V}_k$ is the velocity vector of the kth cable segment in the inertial reference frame

$$\left|\vec{V}_k\right|^2 = \vec{V}_k^T\,\vec{V}_k = \dot{X}_k^2 + \dot{Y}_k^2 + \dot{Z}_k^2 \qquad (k=1,\dots,n+1),$$

where $\dot{X}_k, \dot{Y}_k, \dot{Z}_k$ are the derivative of (2) with respect to time.

C. Rotational Kinetic Energy

Assuming each element has a null cross moment of inertia, the inertia tensor of the jth segment is diagonal in the local RF. The rotational kinetic energy of the multi-body system can be written as sum of the rotational kinetic energy of its elements:

$$E_{rot} = \frac{1}{2}\sum_{j=1}^{n+1} \vec{\omega}'_j \mathbf{I}_j \vec{\omega}_j = \frac{1}{2}\sum_{j=1}^{n+1}(I_{xj}\omega_{xj}^2 + I_{yj}\omega_{yj}^2 + I_{zj}\omega_{zj}^2) \quad (8)$$

where $\vec{\omega}_j$ is the angular velocity of the jth segment into the local reference frame. This angular velocity is calculated with the rotational matrices R_ϕ, R_θ, R_ψ as in Equation 9.

$$\vec{\omega}_j = \begin{pmatrix} 0 \\ 0 \\ \dot{\psi}_j \end{pmatrix} + R_{\psi_j}\begin{pmatrix} 0 \\ \dot{\vartheta}_j \\ 0 \end{pmatrix} + R_{\psi_j}R_{\vartheta_j}\begin{pmatrix} \dot{\phi}_j \\ 0 \\ 0 \end{pmatrix} \qquad (9)$$

The previous equation can be simplified as reported in Eq. 10.

$$\vec{\omega}_j = \begin{pmatrix} \dot{\vartheta}_j\,s_{\psi_j} + \dot{\phi}_j\,c_{\psi_j}\,c_{\vartheta_j} \\ \dot{\vartheta}_j\,c_{\psi_j} - \dot{\phi}_j\,c_{\vartheta_j}\,s_{\psi_j} \\ \dot{\psi}_j - \dot{\phi}_j\,s_{\vartheta_j} \end{pmatrix} \qquad (10)$$

In Equation 8, I_{zj} is the element moment of inertia with respect to the $z-axis$ of the local RF. Since the cable elements are thin rods, I_{zj} can be neglected. This is not true for the virtual segment corresponding to the UAS, where the inertia moments of the vehicle are imposed.

$$I_{zj} = 0 \quad j = 1,\dots,n$$

From Equation 7 and 8, the total energy kinetic energy is independent by the Euler angle ψ and its the time derivative $\dot{\psi}$ for each segment of the cable ($j = 1,\dots,n$). As a consequence, the Lagrange's Equations are not used to compute the ψ angle. In other words the angle ψ is fixed and set equal to zero, reducing of one the degree of freedom of each element of the cable. This is equivalent to substituting the spherical joint with a universal one. The DOFs of the overall system became $3(n+1) - n = 2n+3$.

D. Generalized Coordinates and Forces

The Euler Angles are used as generalized coordinates. The set is composed by $2n$ angles (ϕ, θ) for the cable segments while three additional angles refer to the UAS virtual segment.

The generalize forces associated with the system generalized coordinates can be calculated applying the virtual work principle. The generalized forces Q'_{q_i} are:

$$Q'_{q_i} = \sum_{k=i}^{n+1}\left\{ F_{x_k}\frac{\partial X_k}{\partial q_i} + F_{y_k}\frac{\partial Y_k}{\partial q_i} + \left(F_{z_k} - m_k g\right)\frac{\partial Z_k}{\partial q_i}\right\} + M_{q_i}$$

for $i = 1,\dots,2n+3$ where $\vec{F}_e^i$ and M_{q_i} are respectively the external forces and moment acting on the kth node and $\vec{r}_k = (X_k, Y_k, Z_k)$ is its Cartesian position with respect to the inertial RF.

For each element of the cable, no moments are applied to the node, so that $M_{\phi_i} = M_{\vartheta_i} = 0$ for $i = 1,\dots,n$. This is not true for the UAS virtual segment which is subjected to the vehicle control moments.

Since the cable's nodes position are independent from the angle ψ, all this partial derivatives are null. The only component of the generalized forces of this generalized coordinate is the moment M_{ψ_i}. Moreover no Lagrange's equations are derived for the cable's segments referred to ψ, so Q'_{ψ_i} exists only for the UAV's virtual segment $i = n+1$:

$$Q'_{\psi_{n+1}} = M_{\psi_{n+1}}$$

E. Aerodynamic Forces

The aerodynamic forces are calculated by cross flow principle as described by [17], in the same way proposed by [21]. Each cable element is schematically considered a cylinder of diameter d and length l_j.

The wind velocity in the inertial RF is given by the vector $\vec{V^w}$. The relative velocity $\vec{V}'_{jr}$ between the jth cable segment and the wind in the jth element's local RF is given by Equation 11,

$$\begin{aligned} \vec{V}_{jr} &= \vec{V^w} - \vec{V}_k \\ \vec{V}'_{jr} &= R_{\phi_j\,\vartheta_j\,\psi_j}V_{jr} \end{aligned} \quad j = 1,\dots,n+1 \qquad (11)$$

where $\vec{V}_k$ is the velocity of jth cable's element in the inertial RF. Let's consider a plane passing through the axis of the cable segment and $\vec{V}'_{jr}$. In this plane the three dimensional problem is reduced to a two dimensional problem. The forces acting on the element in the parallel and perpendicular directions to the cylinder axis (Figure 5) are in Eq. 12.

$$\begin{cases} F_\parallel = Lc_\alpha + Ds_\alpha \\ F_\perp = Ls_\alpha - Dc_\alpha \end{cases} \qquad j = 1,\ldots,n \qquad (12)$$

where L and D are lift and drag on the cable segment (Eq.13) and ρ is the air density.

$$\begin{cases} L = \frac{1}{2}\rho dl_j \left|\vec{V}'_{jr}\right|^2 C_l \\ D = \frac{1}{2}\rho dl_j \left|\vec{V}'_{jr}\right|^2 C_d \end{cases} \qquad j = 1,\ldots,n \qquad (13)$$
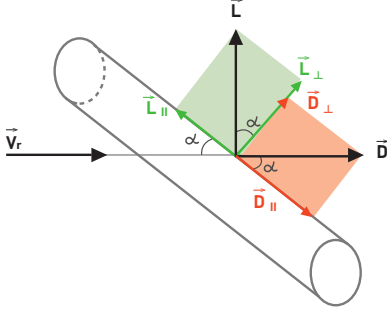

Fig. 5: Cylindrical cable segment invested by the wind

Lift and drag coefficients C_l and C_d are computed according to [17]:

$$\begin{aligned} C_l &= C_{d0}\, s_\alpha^2\, c_\alpha \\ C_d &= C_{d0}\, s_\alpha^3 + \pi C_f \end{aligned} \qquad j = 1,\ldots,n \qquad (14)$$

where C_{d0} is the drag coefficient and C_f is the frictional coefficient.

Substituting equations (13) and (14) in (12), it results:

$$\begin{cases} F_\parallel = \frac{1}{2}\rho dl_j \left|\vec{V}'_{jr}\right| V_\parallel \pi C_f \\ F_\perp = \frac{1}{2}\rho dl_j V_\perp \left(|V_\perp| C_{d0} + \left|\vec{V}'_{jr}\right| \pi C_f\right) \end{cases} \quad j = 1,\ldots,n$$

where $V_\parallel = -\left|\vec{V}'_{jr}\right| c_\alpha$ and $V_\perp = \left|\vec{V}'_{jr}\right| s_\alpha$.

The aerodynamic forces are expressed in the local RF observing that $V'_{jrx} = V_\perp c_\beta$, $V'_{jry} = V_\perp s_\beta$ and $V'_{jrz} = V_\parallel$, where β is the angle between the considered plane and the x axis of the element's local RF. In the jth local RF, $\vec{F}'_j$ is

$$\begin{cases} F'_{jx} = F_\perp c_\beta = \frac{1}{2}\rho dl_j V'_{jrx}\left(|V_\perp| C_{d0} + \left|\vec{V}'_{jr}\right| \pi C_f\right) \\ F'_{jy} = F_\perp s_\beta = \frac{1}{2}\rho dl_j V'_{jry}\left(|V_\perp| C_{d0} + \left|\vec{V}'_{jr}\right| \pi C_f\right) \\ F'_{jz} = F_\parallel = \frac{1}{2}\rho dl_j \left|\vec{V}'_{jr}\right| V'_{jrz} \pi C_f \end{cases}$$

for $j = 1,\ldots,n$, where $|V_\perp| = \sqrt{V'^2_{jrx} + V'^2_{jry}}$ and $\left|\vec{V}'_{jr}\right| = \sqrt{V'^2_{jrx} + V'^2_{jry} + V'^2_{jrz}}$.

For the UAV virtual segment $j = n+1$ the aerodynamic forces in the local RF are the following:

$$\begin{cases} F'_{n+1x} = \frac{1}{2}\rho A_x V'_{n+1rx}\left|V'_{n+1rx}\right| C_{dx} \\ F'_{n+1y} = \frac{1}{2}\rho A_y V'_{n+1ry}\left|V'_{n+1ry}\right| C_{dy} \\ F'_{n+1z} = \frac{1}{2}\rho A_z V'_{n+1rz}\left|V'_{n+1rz}\right| C_{dz} \end{cases}$$

where (A_x, A_y, A_z) and (C_{dx}, C_{dy}, C_{dz}) are respectively the area in the perpendicular plane or the relative axis and the drag coefficient [8].

In the inertial RF, the aerodynamic forces can be evaluated given the the rotational matrix $\vec{F}_j = R^{-1}_{\phi_j \vartheta_j \psi_j} \vec{F}'_j$.

F. Complete Lagrange's Equations

The overall system is described by the matrix expression in Eq. 15. This is the same approach used by the authors in [10] and [16].

$$\mathbf{A}\begin{pmatrix}\ddot{\phi}\\\ddot{\theta}\\\ddot{\psi}\end{pmatrix} + \left[\mathbf{B}\cdot\begin{pmatrix}\dot{\phi}\\\dot{\theta}\\\dot{\psi}\end{pmatrix} + \mathbf{D}\right]\begin{pmatrix}\dot{\phi}\\\dot{\theta}\\\dot{\psi}\end{pmatrix} + \mathbf{C}\begin{pmatrix}\dot{\phi}\dot{\theta}\\\dot{\phi}\dot{\psi}\\\dot{\theta}\dot{\psi}\end{pmatrix} = \begin{pmatrix}\mathbf{Q}^{tot}_\phi\\\mathbf{Q}^{tot}_\theta\\\mathbf{Q}_\psi\end{pmatrix} \tag{15}$$

where

$$\mathbf{Q}^{tot}_\phi = \mathbf{Q}_\phi + \mathbf{Q}''_\phi$$
$$\mathbf{Q}^{tot}_\theta = \mathbf{Q}_\theta + \mathbf{Q}''_\theta$$

$\mathbf{Q}_\phi$, $\mathbf{Q}_\theta$ and $\mathbf{Q}_\psi$ are the generalized forces (6) and $\mathbf{Q}''_\phi$, $\mathbf{Q}''_\theta$ contain the terms due to the cable variable length, proportional to $\ddot{l}_1$.
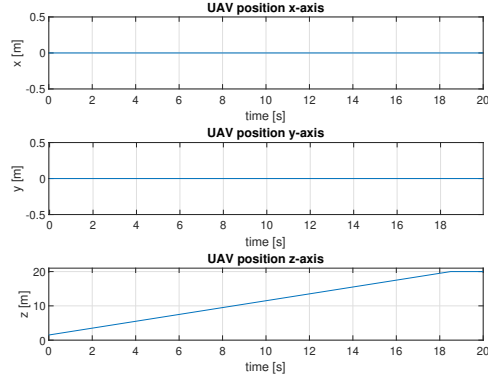
IV. SIMULATIONS

The proposed model is implemented in Matlab/Simulink. Five simulations with different operational conditions are investigated and summarized in Table I. The UAS mass is equal to 25 kg, the simulation time step is 0.0001 s and the length of each element of the cable is equal to 1.5 m, as reported in [21]. This value allows a reasonable balance between simulation cost and details.

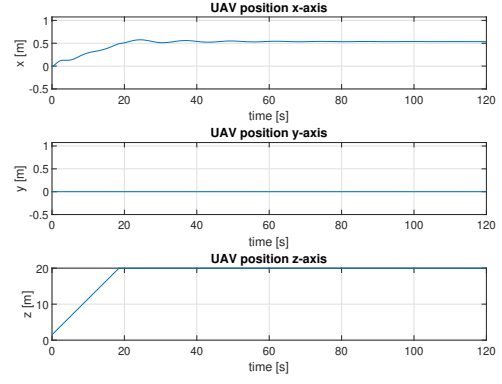| Sim #	Z_{ref} [m]	$Z_{initial}$ [m]	Wind Speed $[V^w_x, V^w_y, V^w_z]$
1	20	0	[0, 0, 0]
2	20	0	[5, 0, 0]
3	20	20	[5, 0, 0]
4	20	20	[10, 0, 0]
5	20	20	[2.5, 2.5, 0]

TABLE I: Simulations profile

A. UAS take-off with no wind
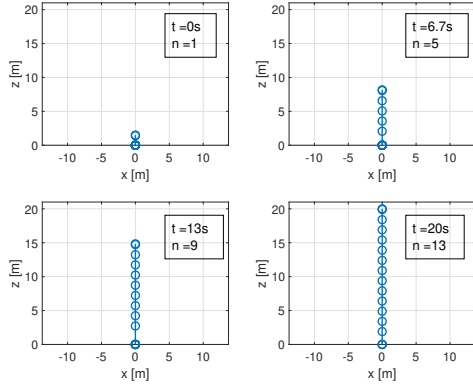
The simulation starts with the vehicle on ground and no wind. The cable is unwound at the velocity of $\dot{l}_1 = 1m/s$. As described above $\dot{l}_1$ is imposed from the outside to the UAS model therefore the quad-rotor rate of climb is limited by this value. A constant unwinding cable velocity is assumed. A reference altitude of 20 m is set so that the vehicle altitude increases linearly. Figure 6b shows the cable extension at different simulation time. The circles represent the junction points between two consecutive cable segments; the last
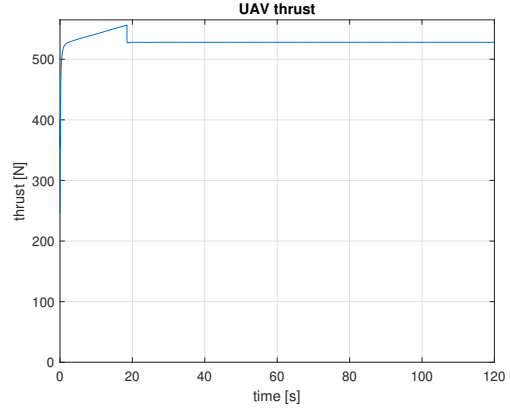
(a) Vehicle position

(b) Cable unwinding

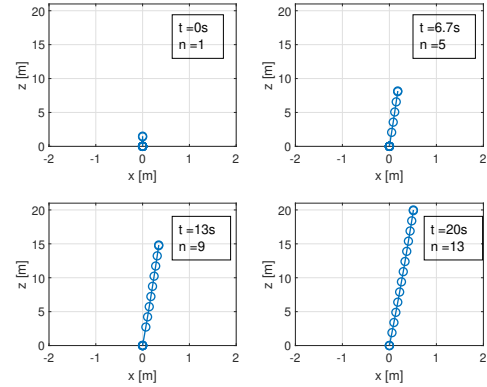Fig. 6: Tethered UAS in no wind conditions during take-off - Simulation 1.

element is the UAS virtual element. The vehicle reaches the reference altitude (20m) after 18.5s (Fig. 6a) and $\dot{l}_1$ is instantaneously set to zero. No wind is acting on the system so that the vehicle x and y positions remain equal to zero. The total number of elements involved in the cable is reported to show the system is able to manage a variable cable length.

B. UAS take-off with 5 m/s wind speed

Initial conditions of this simulation are the same as for the previous one with the only exception of a wind speed along the inertial RF X axis equal to 5m/s. As a consequence, the UAS moves to positive X under the effect of the wind as no position control loop is implemented. Moreover, the vehicle can not reach the command altitude $Z_{Ref} = 20m$. The error between the reference altitude and the actual remain positive. The PID altitude's control is not able to reduce UAV thrust. The controller integrative component requires a negative error value in order to decrease. The UAV thrust is reflected into the cable tension.

C. Hovering with 5 and 10 m/s wind speeds

The simulation starts with the UAS hovering at 20 m above ground. Moreover, a constant wind speed (5 m/s along the IRF X axis) is introduced. The aerodynamics forces acting
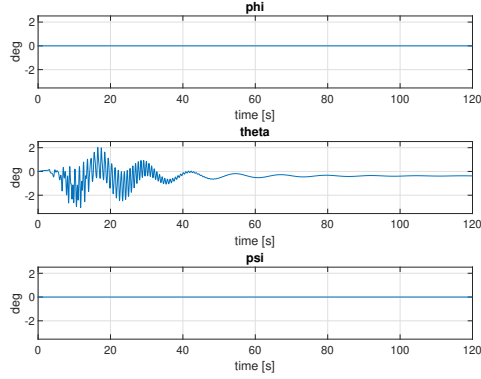

(a) Vehicle position

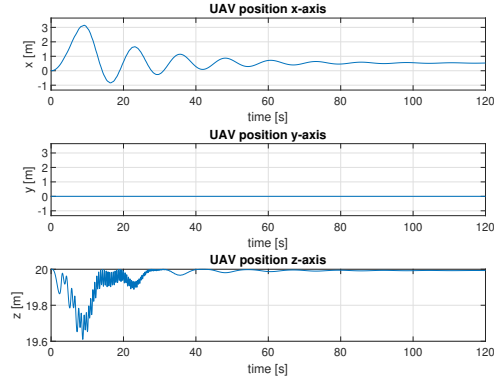(b) UAV thrust force

(c) Cable unwinding

Fig. 7: Tethered UAS simulation with wind during take-off - Simulation 2.

on the cable and the vehicle are responsible for a variation of the pitch angle ϑ, as in Figure 8a. Moreover, due to the wind the UAS is not able to keep a constant position and it moves toward the wind's direction (fig. 8b). Finally, the cable dynamic behaviour is in Figure 8c. It is important to recall that the cable is assumed in-extensible. As a consequence of the wind speed, the cable bends and the vehicle altitude decreases during the transient. Then, a new equilibrium point
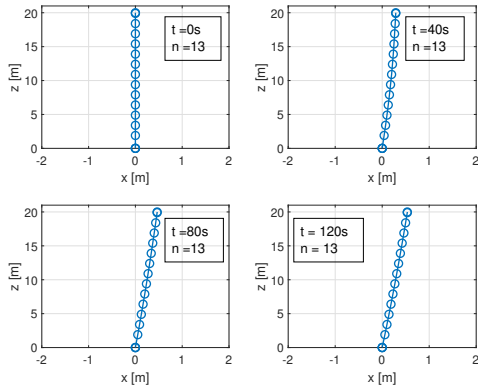
is reached by the system with steady state altitude and pitch errors. Higher wind speeds ($10m/s$ - as for Simulation 4) result in unstable cable behaviour and the simulation breaks. The reason is related to the singularity condition $\vartheta = \frac{\pi}{2}$ of the Euler Angle occurring for the cable element near ground.
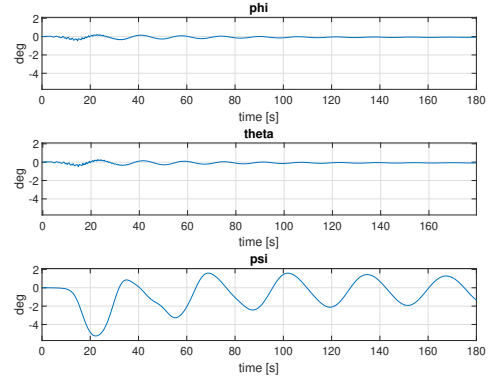

(a) UAV attitude

(b) UAV position

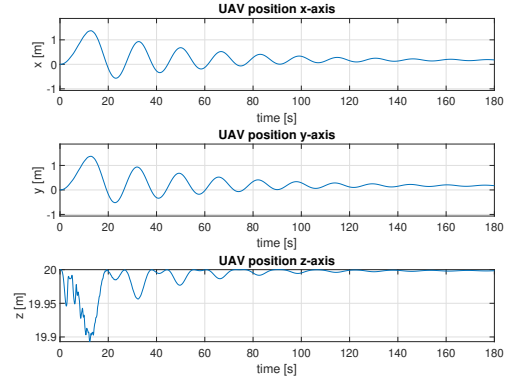(c) Cable behaviour in the X and Z directions

Fig. 8: Simulation results for UAS hovering in wind conditions - Simulation 3.

The stronger the wind the more the first element is prone to align with the ground due to the constraint given in the connection point.
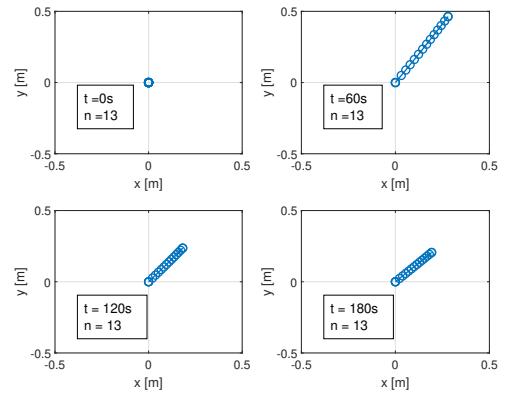
D. Hovering with constant wind speed in X and Y directions

(a) UAV attitude

(b) UAV position

(c) Cable position in *XY* plane

Fig. 9: Simulation results for UAS hovering with constant wind in both X and Y directions - Simulation 5.

In the following simulation, the UAS is hovering while a constant wind speed is acting along IRF X and Y axes. As shown in Figure 9a, the attitude of the vehicle is affected by the wind. When the transient ends, a new equilibrium is found with limited ϕ and θ angle errors. At the same time, a constant position error is shown in Figure 9b as the autopilot is not able to compensate the effect of the wind.

V. CONCLUSIONS

A tethered UAS simulation model is presented and discussed. The Finite Elements Method (FEM) is used to evaluate the dynamic behavior of the system. The cable consists of n segments linked to each other by a spherical joint. The length of the first segment is not constant in order to model a variable cable length to simulate UAS take-off or landing operations. An additional virtual element is used to simulate the unmanned vehicle. The Lagrange's Equations are derived to describe the dynamics of the complete system. Thrust and torque generated by the propellers are computed using the Blade Element Theory. Moreover, aerodynamic forces due to wind are introduced as external disturbances acting on the cable and UAV. Simulation results corroborate the proposed model is able to simulate the system in both wind and still air conditions. The main limitation of the model is given by the representation of the cable segment orientations based on the Euler Angles. Gimbal lock occurs when high wind speed are set as a consequence of the first element alignment with the ground plane ($\theta = \pm\pi/2$). Future works include decoupling the dynamics of the UAS from the cable leveraging a visco-elastic connection. Moreover, a detailed mathematical model for the UAS will be introduced, in addition to the implementation of a position controller for the aerial vehicle. Moreover, a simplified winch model will be proposed to control the tension and extraction velocity of the cable as a function of the UAS operations. Finally, simulation computational effort will be evaluated in order to define an optimal balance between the number of elements in the cable and simulation cost.

REFERENCES

[1] Shakhatreh, H., Sawalmeh, A. H., Al-Fuqaha, A., Dou, Z., Almaita, E., Khalil, I., & Guizani, M. (2019). Unmanned aerial vehicles (UAVs): A survey on civil applications and key research challenges. IEEE Access, 7, 48572-48634.

[2] Alvear, O., Zema, N. R., Natalizio, E., & Calafate, C. T. (2017). Using UAV-based systems to monitor air pollution in areas with poor accessibility. Journal of Advanced Transportation, 2017.

[3] Samir Labib, N., Danoy, G., Musial, J., Brust, M. R., & Bouvry, P. (2019). Internet of Unmanned Aerial Vehicles—A Multilayer Low-Altitude Airspace Model for Distributed UAV Traffic Management. Sensors, 19(21), 4779.

[4] Eltner, A., Sardemann, H., & Blaskow, R. (2019, January). Unmanned aerial and water vehicle data for hydro-morphological river monitoring. In Geophysical Research Abstracts (Vol. 21).

[5] Lussier, M. E., Bradley, J. M., & Detweiler, C. (2019). Extending Endurance of Multicopters: The Current State-of-the-Art. In AIAA Scitech 2019 Forum (p. 1790).

[6] Sri, Karthik Reddy Buchireddy, Aneesh, Poondla, Bhanu, Kiran, & Natarajan, M. (2016). Design Analysis of Solar-Powered Unmanned Aerial Vehicle. Journal of Aerospace Technology and Management, 8(4), 397-407.

[7] Swider-Lyons, K., Stroman, R. O. N., Gould, B. D., Rodgers, J. A., Mackrell, J., Schuette, M., & Page, G. (2014). Hydrogen fuel cells for small unmanned air vehicles. Ecs Transactions, 64(3), 963-972.

[8] Laura Novaro Mascarello, 'Analysis and development of harmless sUAS (small Unmanned Aerial Systems)', Politecnico di Torino, 2018.

[9] Young-il Choo and Mario J. Casarella, 'A Survey of Analytical Methods for Dynamic Simulation of Cable-Body Systems.', Journal of Hydronautics, vol. 7, no. 4, pp. 137–144, 1973, doi: 10.2514/3.62948.

[10] Donald T. Greenwood, Advanced Dynamics. Cambridge University Press, 2003.

[11] M. Bangura, 'Aerodynamics and Control of Quadrotors', The Australian National University, 2017.

[12] M. Bangura, M. Melega, R. Naldi, and R. Mahony, 'Aerodynamics of Rotor Blades for Quadrotors', Jan. 2016.

[13] Marco Tognon, 'Attitude and Tension Control of a Tethered Formation of Aerial Vehicles', University of Pauda, 2014.

[14] Joshua T. Mfiri, Johann Treurnicht, and Jacobus A.A. Engelbrecht, 'Automated Landing of a Tethered Quad-Rotor UAV with Constant Winching Force', presented at the 2016 Pattern Recognition Association of South Africa and Robotics and Mechatronics International Conference (PRASA-RobMech), Stellenbosch, South Africa.

[15] Kurt A. Talke, Mauricio de Oliveira, and Thomas Bewley, 'Catenary Tether Shape Analysis for a UAV - USV Team', presented at the IEEE/RSJ International Conference on Intelligent Robots and Systems (IROS), Madrid, Spain, October 1-5, 2018, pp. 7803–7809.

[16] A. A. Shabana, Dynamics of multibody systems, 4th ed. Cambridge: Cambridge University Press, 2013.

[17] Sighard F. Hoerner, 'Fluid-Dynamic Drag: Practical Information on Aerodynamic Drag and Hydrodynamic Resistance'. Midland Park, N.J., 1965.

[18] Taeyoung Lee, 'Geometric Controls for a Tethered Quadrotor UAV', presented at the 2015 IEEE 54th Annual Conference on Decision and Control (CDC), December 15-18, 2015. Osaka, Japan, vol. 15, pp. 2749–2754.

[19] S. Puneet, D. Mortari, and J. Junkins, 'How to avoid singularity when using Euler angles?', Advances in the Astronautical Sciences, vol. 119, pp. 1409–1426, Jan. 2005.

[20] M. Krznar, D. Kotarski, P. Piljek, and D. Pavkovic, 'On-line Inertia Measurement of Unmanned Aerial Vehicles using on board Sensors and Bifilar Pendulum', Interdisciplinary Description of Complex Systems, vol. 16, pp. 149–161, 2018, doi: 10.7906/indecs.16.1.12.

[21] Sina Doroudgar, 'Static and Dynamic Modeling and Simulation of the Umbilical Cable in A Tethered Unmanned Aerial System', SIMON FRASER UNIVERSITY, 2016.

[22] Peter Juhl Savnik, 'Tether Control for Unmanned Aerial Vehicle', Technical University of Denmark, 2015.

[23] Piero Graziano Ioppo, 'The Design, Modelling and Control of an Autonomous Tethered Multirotor UAV', University of Stellenbosch, 2017.

[24] Frédéric Muttin, 'Umbilical deployment modeling for tethered UAV detecting oil pollution from ship', Applied Ocean Research, vol. 33, pp. 332–343, 2011, doi: 10.1016/j.apor.2011.06.004.

[25] D. Ferreira de Castro, J. S. Santos, M. Batista, D. Antônio dos Santos, and L. C. Góes, 'Modeling and Control of Tethered Unmanned Multicopters in Hovering Flight', in AIAA Modeling and Simulation Technologies Conference, Dallas, TX, 2015, doi: 10.2514/6.2015-2333.

[26] Marco Tognon, 'Attitude and Tension Control of a Tethered Formation of Aerial Vehicles', University of Pauda, 2014.

[27] C. M. Ablow and S. Schechter, 'Numerical simulation of undersea cable dynamics', Ocean Engineering, vol. 10, no. 6, pp. 443–457, Jan. 1983, doi: 10.1016/0029-8018(83)90046-X.

[28] J. W. Kamman and Ronald L. Huston, 'Modeling of Variable Length Towed and Tethered Cable System', Journal of Guidance, Control, and Dynamics, vol. 22, no. 4, Aug. 1999.

[29] V. K. Srivastava, Y. Sanyasiraju, and M. Tamsir, 'Dynamic Behavior of Underwater Towed-cable in Linear Profile', International Journl of Scientific & Engineering Researh, vol. 2, no. 7, p. 10, July2011.

[30] O. O. Ajayi and O. O. Aribike, 'MODELLING AND SIMULATION OF SUBSEA UMBILICAL DYNAMICS: A NUMERICAL APPROACH', International Journal of Computer Thechniques, vol. 2, no. 1, p. 12, 2015.

[31] Mai The Vu, Choi Hyeung-Sik, Kim Joon-Young, Dae-Hyeung Ji, Hyun-Joong Son, and Tran Ngoc Huy, 2016. 'A Study on the Dynamics of Marine Umbilical Cable for Underwater Vehicle' doi: 10.1007/978-3-319-27247-4.49.

[32] 'Design and Use of Professional Drones.' Eagle Sky Light. Retrieved April, 2020 from eagleskylight.it/en/.